This is an open access article published under an ACS AuthorChoice License, which permits copying and redistribution of the article or any adaptations for non-commercial purposes.

ACS Photonics

Article

pubs.acs.org/journal/apchd5

Sensitive, Fast, and Stable Perovskite Photodetectors Exploiting Interface Engineering

Brandon R. Sutherland,‡ Andrew K. Johnston,‡ Alexander H. Ip, Jixian Xu, Valerio Adinolfi, Pongsakorn Kanjanaboos, and Edward H. Sargent*

Department of Electrical and Computer Engineering, University of Toronto, 35 St. George Street, Toronto, Ontario M5S 1A4, Canada

Supporting Information

ABSTRACT: Organometallic halide perovskites are a class of solution-processed semiconductors exhibiting remarkable optoelectronic properties. They have seen rapid strides toward enabling efficient third-generation solar cell technologies. Here, we report the first material-tailoring of TiO_2/perovskite/spiro-OMeTAD junction-based photodiodes toward applications in photodetection, a field in need of fast, sensitive, low-cost, spectrally tunable materials that offer facile integration across a broad range of substrates. We report photodetection that exhibits 1 μs temporal response, and we showcase stable operation in the detection of over 7 billion transient light pulses through a continuous pulsed-illumination period. The perovskite diode photodetector has a peak responsivity approaching 0.4 A W^{-1} at 600 nm wavelength, which is superior to red light detection in crystalline silicon photodiodes used in commercial image sensors. Only by developing a composite Al_2O_3/PCBM front contact interface layer were we able to stabilize device operation in air, reduce dark current, and enhance the responsivity in the low-bias regime to achieve an experimentally measured specific detectivity of 10^{12} Jones.

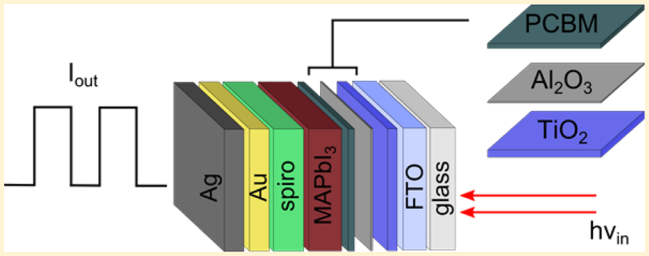

KEYWORDS: *perovskites, photodetectors, specific detectivity, dark current, photodiodes*

Perovskites of the form $CH_3NH_3PbX_{3-x}Y_x$ ($MAPbX_{3-x}Y_x$ for short), where X and Y include halides from the list I, Br, and Cl, are spectrally tunable from 390−790 nm,[1] possess a direct bandgap exhibiting a steep absorption edge,[2] and have demonstrated remarkable efficiency in photogenerated charge collection. As a result, they have achieved certified photovoltaic power conversion efficiencies reaching 20.1%.[3] This rapid and impressive progress in solar harvesting has also spawned the exploration of diverse applications of perovskite thin films across the domain of semiconductor devices. Perovskite active layers have now enabled high-brightness light emitting diodes,[4] optically pumped lasers,[5−7] and efficient solar-powered water splitting systems.[8] Recently, perovskites have been investigated for their prospects in light sensing as photodetectors.[9−15]

Photodetectors are evaluated based on responsivity, speed, and sensitivity. Responsivity is the output photocurrent, I_{out}, divided by the incident optical power, P_{in}, $R = I_{out}/P_{in}$ (A W^{-1}). Speed is judged from the rise and fall response times, t_r and t_f, respectively, of a transient photocurrent. Sensitivity measures the ability to detect a weak light signal and is reported as specific detectivity, $D^* = R\,(A\cdot\Delta f)^{1/2}\,I_{noise}^{-1}$ (Jones, cm $Hz^{1/2}$ W^{-1}). Devices with higher responsivity and a smaller noise current can achieve a signal-to-noise ratio of 1, which corresponds to the noise-equivalent intensity (i.e., the detection limit) at a lower incident intensity. Specific detectivity is normalized to device area, A, and the frequency bandwidth, Δf, enabling comparison among different device architectures, areas, and measurement bandwidths.

Many advances in high-efficiency perovskite photovoltaic cells have exploited mesostructured n-i-p TiO_2/perovskite/spiro-OMeTAD semiconductor junctions; however, for applications in photodetection, planar devices are of considerable interest in light of their potential for a high degree of pixel-to-pixel uniformity. Prior efforts on developing perovskite photodiodes for photosensing have primarily focused on planar p-i-n architectures with an organic front electrode.[12,13] Here, we began from the principle that the excellent quantum efficiency of n-i-p perovskite photodiodes could also be leveraged in planar large-area pixels for photodetection. The higher work function top electrodes in these devices compared to their p-i-n counterparts are of continued interest to the perovskite optoelectronic device community. We would strive to use materials stack control to customize the device to this application, maximizing responsivity and minimizing the dark current for improved sensitivity in light detection.

The best perovskite solar light harvesting devices achieve an open-circuit voltage, V_{oc}, of 1.1 V,[16] a short-circuit current density, J_{sc}, of 20 mA cm^{-2},[16] and a diode ideality factor, n, of 2.[17] From this, the reverse saturation current density of the diode, J_0, is estimated to be on the order of 10 pA cm^{-2} from

Received: March 30, 2015
Published: June 18, 2015

Downloaded via SICHUAN UNIV on December 26, 2024 at 02:04:34 (UTC).
See https://pubs.acs.org/sharingguidelines for options on how to legitimately share published articles.

$V_{oc} = nkTq^{-1} \ln(J_{sc}/J_0 + 1)$, where k is Boltzmann's constant, T is the temperature, and q is the electronic charge. In reality, the total dark current density, J_{dark}, includes both the aforementioned contribution from J_0 and also any parallel shunt path currents. In non-ideal perovskite photovoltaic cells having a finite shunt resistance, R_{sh}, the open-circuit voltage is given by $V_{oc} = nkTq^{-1} \ln([J_{sc} - V_{oc}/R_{sh}]/J_0 + 1)$. Shunt paths do not play a critical role in limiting V_{oc} until R_{sh} becomes extremely small. A shunt path with a resistance of 1 kΩ cm^2 will only reduce the theoretical V_{oc} of a perovskite solar cell from 1.1 to 1.0971 V; however, shunt paths of this magnitude can immensely increase the net dark current under reverse bias. For example, a 0.1 V potential difference across this shunt carries a current of 0.1 mA cm^{-2}, which is a 10^7 fold increase over the 10 pA cm^{-2} theoretical minimum.

As a result, past highly successful work to optimize solar cell performance does not necessarily ensure that dark currents will be compellingly low for photodetection. In photodetectors, because D^* scales with $J_{dark}^{-1/2}$, it is imperative to investigate materials strategies that systematically minimize dark current in light sensors via materials stack engineering.

We therefore set about measuring and then minimizing the dark current of perovskite diodes. Seeking to minimize leakage associated with physical shunts that involved direct TiO_2/spiro-OMeTAD physical connections, we focused on developing an electron-accepting composite electrode. We endeavored to produce a thin, pinhole-free compact layer of Al_2O_3, electing to apply it via atomic layer deposition (ALD) onto the nanostructured TiO_2. This strategy has previously been reported in electroluminescent devices to enhance radiative efficiency[4] and has been postulated to passivate TiO_2 surface trap states.[18] To explore a further means of suppressing dark current, we added a thin layer of phenyl-C_{61}-butyric acid methyl ester (PCBM, a fullerene derivative), which we posited might provide further advantages as an additional hole-blocking barrier atop TiO_2 (where the latter can exhibit hole traps at interfaces that may serve as recombination, and thus generation, centers contributing to dark current). PCBM has also been shown to passivate interface charge trap states at perovskite semiconductor junctions[19,20] and in perovskite polycrystalline grain boundaries.[21] The use of PCBM further provides an added degree of freedom in the selection of the amplitude of the barrier to back-injection from TiO_2 to $MAPbI_3$.[22]

The architecture that minimized perovskite photodiode dark current is shown in Figure 1a. The flat-band energy alignment is shown in Figure 1b. The energy band diagram is based on literature values for FTO,[23] TiO_2,[24] PCBM,[22] $MAPbI_3$,[2] spiro-OMeTAD,[2] and Au.[23] The dark current density, J_{dark}, from 0 V to −0.5 V, a typical operating regime for a low-noise, low-voltage photodiode, is shown for three cases in Figure 1c: TiO_2 alone, with the addition of Al_2O_3, and with the further addition of PCBM. These three cases are designated as photodiodes I1, I2, and I3, respectively, and this terminology is used throughout the manuscript. When ALD Al_2O_3 and PCBM are combined, the dark current is reduced by 1 order of magnitude compared to the reference case (conventional TiO_2 to $MAPbI_3$ junction). The thicknesses of each interface layer were optimized to maximize the ratio of responsivity over dark current density (Figure S1, Supporting Information (SI)).

The spectral responsivity at zero bias is reported in Figure 2a. Perovskite thin films are remarkably efficient light absorbers, highlighting their promise for high-responsivity photodiodes.

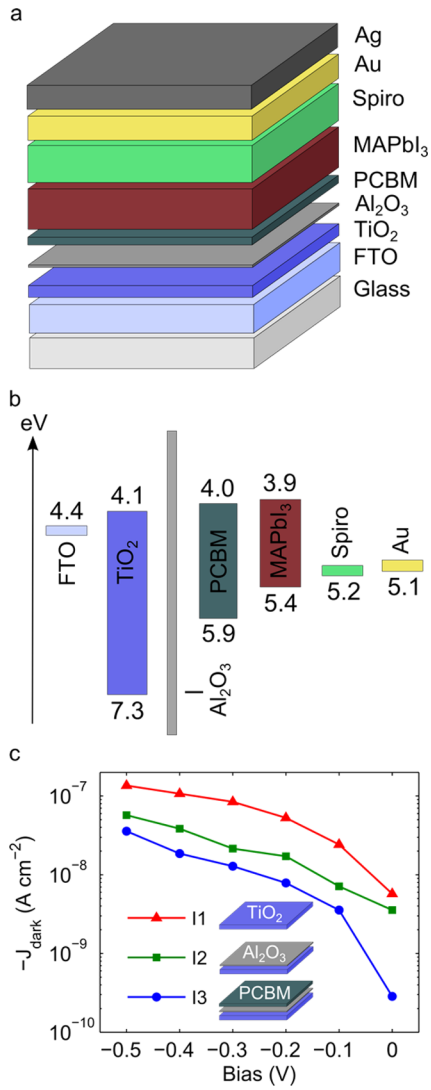

Figure 1. Perovskite diode photodetector architecture and dark characteristics. (a) Device material stack; the approximate thickness of each layer from FTO to Ag is 200, 50, 1, 10, 250, 200, 100, and 100 nm. (b) Energy band alignment of the device material stack. (c) Effect of the front contact material stack on the dark current density. The addition of Al_2O_3 and further addition of PCBM reduce the dark current. The notations and color scheme for I1, I2, and I3 are used throughout the manuscript.

The addition of the interface layers in devices I2 and I3 improves the responsivity in the green and red regions (560–660 nm) as well as the near-infrared at 750 nm. The increases in responsivity are consistent with the posited passivation of charge-trapping recombination centers at the interface. Device I3 achieves a peak responsivity as high as 0.395 A W^{-1} at 600 nm wavelength. This is comparable to commercial large-area silicon photodiodes detecting at the same wavelength[25] and superior to typical thin-photodiode silicon complementary-metal-oxide-semiconductor (CMOS) pixels in the red wavelength range.[26] Here, the strong direct-bandgap absorption of perovskites enables them to outperform crystalline silicon, which has weaker absorption near its direct-to-indirect transition.

In contrast to devices I1 and I2, photodiode I3 exhibits bias-independent responsivity (Figure 2b), even down to zero bias. This is a result of efficient minority carrier diffusion in the

DOI: 10.1021/acsphotonics.5b00164
ACS Photonics 2015, 2, 1117−1123

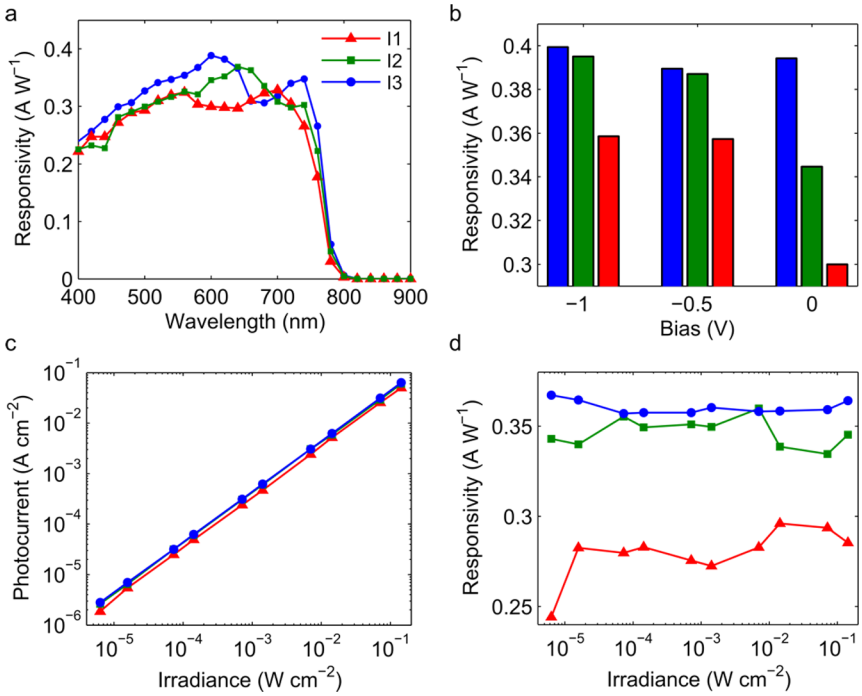

Figure 2. Responsivity measurements. (a) Spectral responsivity at zero bias with 0.1 mW cm^{-2} irradiance. The responsivity sharply increases above the bandgap of $MAPbI_3$ at 780 nm. The responsivity in the green and red (560−660 nm) and in the near-infrared at 750 nm is enhanced with the addition of Al_2O_3 and PCBM. (b) Responsivities at 0, −0.5, and −1 V bias at 600 nm wavelength with 0.1 mW cm^{-2} input irradiance. The interface stack greatly improves the zero bias responsivity with device I3 being bias-insensitive. (c) Photocurrent linearity upon varying the 640 nm input irradiance at 0 V bias. (d) Responsivity dependence on input irradiance at 640 nm with 0 V bias. For devices I2 and I3, the input irradiance is flat over 4 decades, corresponding to a dynamic range exceeding 80 dB.

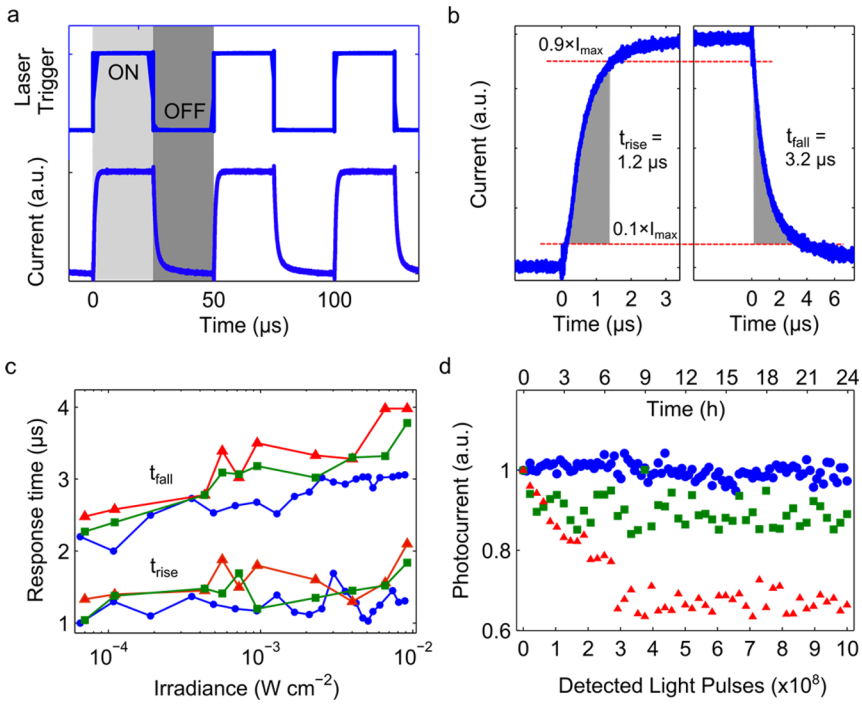

Figure 3. Perovskite photodetector speed at 0 V bias. (a) Transient current output of device I3 to a time-varying input light signal (640 nm, 50 μs period square wave, 20 mW cm^{-2} peak-to-peak). (b) Photocurrent rise and fall of device I3 at an input irradiance of 20 mW cm^{-2}. Laser pulse is triggered on (rise)/off (fall) at time t = 0. (c) Rise and fall time dependence on input irradiance for all devices. On average, device I3 is the fastest and least dependent on input irradiance. d) Device stability in air under continuous illumination (640 nm, 40 μs period square wave, 100 μW cm^{-2} peak-to-peak). Photocurrent of device I3 is stable over 24 h, after the detection of one billion laser pulses. Device I2 experiences an initial decay in photocurrent to 90% of its initial value, and device I1 experiences gradual photocurrent decay to 60% of its initial value.

DOI: 10.1021/acsphotonics.5b00164
ACS Photonics 2015, 2, 1117−1123

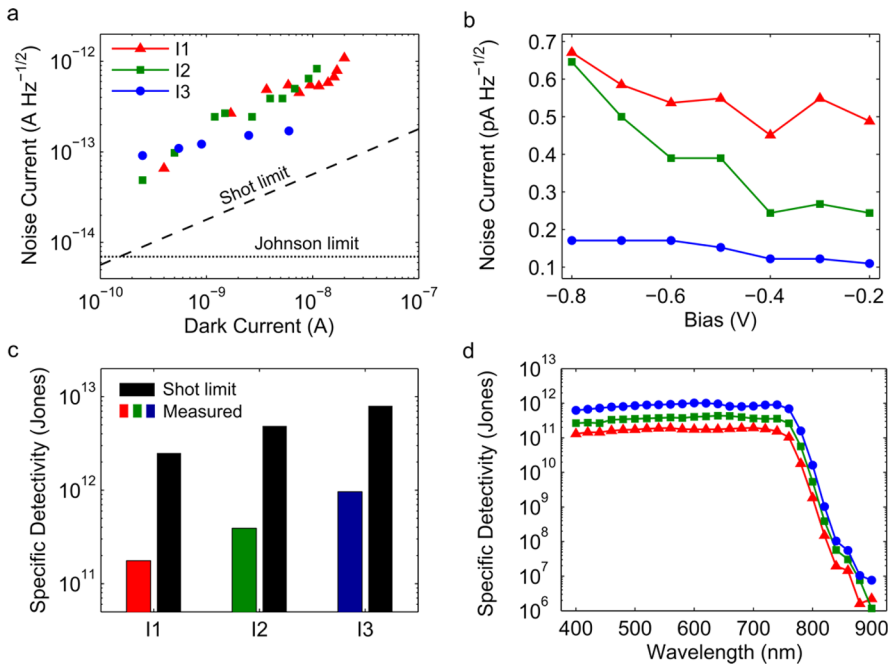

Figure 4. Perovskite photodetector noise current and detectivity. (a) Measurement of noise current. The measured noise current is compared to the theoretical shot and Johnson noise limits. Using our measurement setup, we are able to approach the theoretical shot limit to within an order of magnitude. (b) The noise current dependence on bias. Because of its reduced dark current density, device I3 has the lowest noise current density. (c) Specific detectivity at −0.2 V, 600 nm, and 0.1 mW cm^{-2} compared to the shot limit for each device. (d) Spectral specific detectivity at −0.2 V and 0.1 mW cm^{-2} input irradiance.

perovskite absorber layer being unimpeded by charge trapping at the semiconductor junction. For devices I1 and I2, the external bias provides charge carriers that can fill trap states, enabling photogenerated charges to traverse the junction without impediment. As a result, device I3 operates efficiently at a low reverse bias, thereby producing a lower background current and lower noise. Consistent with the enhanced responsivity at zero bias, device I3 also shows the best performance in photovoltaic mode when operating as a solar cell (Figure S2, SI). To study the device response under varying degrees of input irradiance, we illuminated the samples with an above-bandgap laser at λ = 640 nm. The photocurrent and responsivity of devices I2 and I3 are linear across greater than 4 decades of intensity, corresponding to a linear dynamic range exceeding 80 dB (Figure 2c, d). Device I1 begins to lose response at irradiances near 10 μW cm^{-2}.

To investigate the photodetector speed of response, we illuminated the device using a time-varying square wave light signal having a 50 μs pulse duration and 50% duty cycle. We used the same 640 nm wavelength laser, which can be modulated up to 20 MHz, to obtain the intensity dependence, as shown in Figure 2c and d. Devices I1−I3 exhibit similar response times. Device I3 is marginally faster in sweeping carriers out following illumination. The transient photocurrent response of device I3 (time base referenced to a trigger of the input laser signal) is shown in Figure 3a. The rise and fall times are detailed in Figure 3b. Rise and fall times are defined as the time to transition between 10% of the minimum current to 90% of the maximum, and from 90% down to 10%, respectively. It was previously believed that perovskite photodiodes based on lithium-salt doped hole-transport layers are inherently slow with initial reported response times of 30 ms.[13] The photodiodes in this work exhibit a rise time of 1 μs and a fall time of 3 μs, which is a 10^4 increase over prior work on n-i-p perovskite photodiodes and comparable to the best reported values for perovskite photodetectors.[12,13] In all devices, the fall time is slower than the rise time with the slower component typically attributed to the diffusive contribution to photocurrent during discharging.[27] We hypothesize that variations in the fabrication of the perovskite active film and the TiO_2 and spiro-OMeTAD electrodes between this work and the similar n-i-p device studied in ref 12 may account for the observed differences in device speed.

The dependence of rise and fall times on input irradiance for all photodiode architectures is given in Figure 3c. The devices (I3 in particular) operate near their fastest temporal response over two full decades of input irradiance: the rise time remains consistent over more than 2 orders of magnitude of intensity, whereas the fall time increases from 2 μs to upwards of 3−5 μs.

Perovskite semiconductors demand investigation with respect to their stability over time under illumination and bias. We studied these devices over a 24 h period in air. Figure 3d demonstrates that the output photocurrent of device I3 remains constant over a period of 24 h following the detection of 1 billion light pulses, whereas device I2 experiences an initial decay down to 90% of its initial value, and I1 decays slowly down to 60% of its initial value. The improved stability with the addition of these interface layers may be attributed to physically and electrically separating the (posited to be unstable) TiO_2 and spiro-OMeTAD interfaces in devices I2 and I3. The improved stability is consistent with prior reports employing PCBM, demonstrating a stabilization of photocurrent under solar irradiation,[19] and a stabilization of the dark current at a fixed reverse bias.[21] We have further encapsulated a device of architecture I3 and have demonstrated stability of the photocurrent over a period of 1 week, after the detection of over 7 billion light pulses, in air (Figure S3, SI).

DOI: 10.1021/acsphotonics.5b00164
ACS Photonics 2015, 2, 1117−1123

To evaluate the specific detectivity of the photodetector, we measured the noise current as a function of reverse bias. In the ideal case, the noise current would approach the shot noise limit under reverse bias, and approach the Johnson–Nyquist noise limit as the bias approaches zero. Shot noise associated with the quantized nature of electrons is given by the Poissonian-derived $(2qI_{dark}\Delta f)^{1/2}$, where q is the electronic charge constant, and I_{dark} is the net dark current.[21] Johnson–Nyquist (also referred to as Johnson or thermal noise) is the bias-independent noise associated with thermal excitation of charge carriers in any resistive component at nonzero temperatures and is given by $(4kT\Delta f/R)^{1/2}$, where k is Boltzmann's constant, T is temperature, and R is resistance.[28] The measured noise current is compared relative to the best-case shot noise and Johnson noise limits, shown in Figure 4a. The devices reported herein approached the shot noise limit within less than a factor of 10 under reverse bias. This finding illustrates the need to measure, rather than infer from dark current measurements, the noise and hence the specific detectivity in all photodetectors.

The noise current is shown as a function of bias in Figure 4b. Because of the improvements in dark current density, devices I2 and I3 have reduced noise current. The specific detectivity at −0.2 V and 600 nm wavelength, in reference to the theoretical shot limit, is given for all devices in Figure 4c. The measured D^* values increase with the increase in the theoretical shot limit for each device.

Device I3 achieves a peak D^* of 10^{12} Jones. Sensitivities of this order are comparable to those of commercial silicon photodetectors, whose detectivity typically peaks in the range of 4×10^{12} Jones.[29] The spectral dependence of D^* is given in Figure 4c. D^* of device I3 approaches 10^{12} Jones across the wavelength range 400–780 nm, exhibiting high sensitivity throughout the visible and into the near-infrared region. A statistical analysis of the key figures of merit for each device architecture is summarized in Table S1 in the SI.

Rapid optical absorption and excellent charge transport properties underlie the promising responsivity of these perovskite photodiodes. Their approach to unity quantum yield limit is attractive in a diode that does not require the application of an external bias. Perovskites, due to their facile processing, are inherently compatible with not only large-area devices, such as in this work, but also with pixel-based CMOS readout circuits.[30] The thermal budget required in the processing of perovskites is far below the allowed thermal budget of fully fabricated CMOS circuitry. Therefore, perovskites are a promising candidate for on-chip CMOS incorporation following the silicon back-end.

Further progress in increasing normalized detectivity will focus on reducing the dark current. For their full potential on this front to be reached, perovskite photodiodes—with their impressively high open-circuit voltages up to 1.1 V—are in principle capable of extremely low reverse saturation current densities of 10 pA cm^{-2}. Suppressing dark current further and thereby facilitating even higher D^* values will require added effort toward eliminating sources of shunt paths and ensuring that any such paths remaining are even more highly rectifying. This work suggests substantial promise for perovskite active layers beyond solar energy harvesting and into the realm of sensing applications.

METHODS

TiO_2 Substrate Fabrication. Cleaned glass substrates coated with fluorine-doped tin oxide (TEC 15; Pilkington) were used in this work. TiO_2 (50 nm) was deposited onto these substrates via magnetron sputtering at an argon pressure of 7.5 mTorr at a rate of 0.08 Å s^{-1} with an Angstrom Engineering Åmod deposition system in an Innovative Technology glovebox. The substrates were then treated with a 120×10^{-3} M solution of $TiCl_4$ in a 70 °C oven for 30 min, followed by rinsing with deionized water, and annealing on a 520 °C hot plate for 45 min in ambient air.

Al_2O_3 and PCBM Deposition. In the devices where Al_2O_3 was employed, a 1 nm layer was deposited onto the TiO_2 coated substrates in a Cambridge Nanotech Savannah S100 atomic layer deposition system using Aluminum tris(2,2,6,6-tetramethyl-3,5-heptanedionate) and deionized H_2O as precursors for Al and O, respectively. For both precursors, a pulse duration of 15 ms and a purge time of 20 s was used. The chamber temperature was 150 °C, and the N_2 carrier gas flow rate was 20 sccm. For devices employing PCBM, a 10 mg/mL solution of PCBM was prepared in chlorobenzene. The layer was deposited via spin coating at 4000 rpm for 20 s. The substrate was then annealed for 20 min at 70 °C.

$CH_3NH_3PbI_3$ Perovskite Active Layer Deposition. A solution of PbI_2 (350 mg/mL) was prepared in dimethylformamide (DMF). The layer was deposited via spin coating at 6000 rpm for 30 s. Both substrate and solution were heated to 70 °C prior to deposition. The film was then annealed at 70 °C for 5 min. A solution of methylammonium iodide (40 mg/mL) and a separate solution of methylammonuim chloride (15 mg/mL) were prepared in 2-propanol. The two solutions were mixed in a 2:1 (MAI:MACl) ratio by volume. The resulting solution was deposited using spin coating at 3000 rpm for 30 s. The film was then annealed at 75 °C for 5 min, 100 °C for 10 min, and 150 °C for 10 min.

Spiro-OMeTAD and Au/Ag Deposition. A solution of spiro-OMeTAD (2,2′,7,7′-tetrakis(*N*,*N*-di-4-methoxyphenylamino)-9,9′-spirobifluorene) was synthesized by dissolving spiro-OMeTAD (63 mg/mL) in chlorobenzene. Twenty microliters of 4-*tert*-butylpyridine was added to the solution, followed by 70 μL of a solution (170 mg/mL) of bis(trifluoromethane)sulfonimide lithium salt dissolved in acetonitrile. This solution was deposited via spin-coating at 5000 rpm for 30 s. Au and Ag were deposited in an Angstrom Engineering Å mod deposition system in an Innovative Technology glovebox. Au (100 nm) was deposited via e-beam evaporation at a rate of 1.5 Å s^{-1}, and 100 nm of Ag was deposited via thermal evaporation at a rate of 2.0 Å s^{-1}. The device active area, defined by an evaporation shadow mask, is 0.07 cm^2.

Dark Current Density Measurements. Dark current was measured in air with a Keithley 2400 source meter, which was also used as the bias source.

Photocurrent Measurements. Spectral and bias-dependent responsivity was measured in air by illuminating the device through a 0.049 cm^2 aperture with a collimated 220 Hz chopped light source (450 W xenon lamp through a monochromator with order-sorting filters). The power was measured with a calibrated Newport 818-UV power meter. The photocurrent signal was measured with a Stanford Research Systems lock-in amplifier set to voltage mode. Speed was measured by illuminating the device with a 640 nm Melles–

DOI: 10.1021/acsphotonics.5b00164
ACS Photonics 2015, 2, 1117–1123

Griot (56RCS009/HS) laser diode driven by an Agilent 33120A function generator. The photocurrent was measured in air with an Agilent Infiniium Oscilloscope (DSO8104A) across a 50 Ω input impedance triggered by the laser diode driving pulse. The power was measured with a calibrated Newport 818-UV power meter.

Noise Current Measurements. Noise current was measured in air in a dark and electrically shielded box with a Stanford Research Systems lock-in amplifier set to voltage mode at an internal reference of 220 Hz to match the equivalent noise bandwidth of the responsivity measurements. The input was read across an external series 8.2 MΩ resistor in an electrically shielded enclosure, and bias was applied by a Keithley 2400 source meter in series with the device.

AM 1.5G Solar Cell Measurements. A Keithley 2400 source meter was used as a bias source and to measure current. The AM 1.5G solar spectrum was simulated with a xenon lamp and spectral filters. The spectral mismatch of the system was measured using a calibrated reference solar cell (Newport). The total AM 1.5 spectral mismatch (taking into account the simulator spectrum and the spectral responsivities of the test cell, reference cell, and broadband power meter) was measured to be ∼16.4%. A multiplicative factor of 0.836 was applied to the output current-density of the cell to most accurately represent the true AM 1.5G photocurrent. The uncertainty of the current−voltage measurements was estimated to be ±3.3%.

■ ASSOCIATED CONTENT

Supporting Information

Interface thickness optimizations, photovoltaic performance, long-term stability, and device statistical breakdown. The Supporting Information is available free of charge on the ACS Publications website at DOI: 10.1021/acsphotonics.5b00164.

■ AUTHOR INFORMATION

Corresponding Author

*E-mail: ted.sargent@utoronto.ca.

Author Contributions

‡B.R.S. and A.K.J. contributed equally to this work.

Notes

The authors declare no competing financial interest.

■ ACKNOWLEDGMENTS

This publication is based in part on work supported by an award (KUS-11-009-21) from the King Abdullah University of Science and Technology (KAUST), by the Ontario Research Fund Research Excellence Program, and by the Natural Sciences and Engineering Research Council (NSERC) of Canada. The authors thank Dr. F. Pelayo García de Arquer for helpful discussion regarding noise current measurements and Dr. Michael Saliba for consultation on perovskite device processing.

■ REFERENCES

(1) Xing, G.; Mathews, N.; Lim, S. S.; Yantara, N.; Liu, X.; Sabba, D.; Grätzel, M.; Mhaisalkar, S.; Sum, T. C. Low-Temperature Solution-Processed Wavelength-Tunable Perovskites for Lasing. *Nat. Mater.* **2014**, *13*, 476−480.

(2) Kim, H.-S.; Lee, C.-R.; Im, J.-H.; Lee, K.-B.; Moehl, T.; Marchioro, A.; Moon, S.-J.; Humphry-Baker, R.; Yum, J.-H.; Moser, J. E.; Grätzel, M.; Park, N.-G. Lead Iodide Perovskite Sensitized All-Solid-State Submicron Thin Film Mesoscopic Solar Cell with Efficiency Exceeding 9%. *Sci. Rep.* **2012**, *2*.

(3) Research Cell Efficiency Records, NREL. http://www.nrel.gov/ncpv/ (accessed March, 2015).

(4) Tan, Z.-K.; Moghaddam, R. S.; Lai, M. L.; Docampo, P.; Higler, R.; Deschler, F.; Price, M.; Sadhanala, A.; Pazos, L. M.; Credgington, D.; Hanusch, F.; Bein, T.; Snaith, H. J.; Friend, R. H. Bright Light-Emitting Diodes Based on Organometal Halide Perovskite. *Nat. Nanotechnol.* **2014**, *9*, 687−692.

(5) Sutherland, B. R.; Hoogland, S.; Adachi, M. M.; Wong, C. T. O.; Sargent, E. H. Conformal Organohalide Perovskites Enable Lasing on Spherical Resonators. *ACS Nano* **2014**, *8*, 10947−10952.

(6) Deschler, F.; Price, M.; Pathak, S.; Klintberg, L. E.; Jarausch, D.-D.; Higler, R.; Hüttner, S.; Leijtens, T.; Stranks, S. D.; Snaith, H. J.; Atatüre, M.; Phillips, R. T.; Friend, R. H. High Photoluminescence Efficiency and Optically Pumped Lasing in Solution-Processed Mixed Halide Perovskite Semiconductors. *J. Phys. Chem. Lett.* **2014**, *5*, 1421−1426.

(7) Zhang, Q.; Ha, S. T.; Liu, X.; Sum, T. C.; Xiong, Q. Room-Temperature Near-Infrared High-Q Perovskite Whispering-Gallery Planar Nanolasers. *Nano Lett.* **2014**, *10*, 687−692.

(8) Luo, J.; Im, J.-H.; Mayer, M. T.; Schreier, M.; Nazeeruddin, M. K.; Park, N.-G.; Tilley, S. D.; Fan, H. J.; Gratzel, M. Water Photolysis at 12.3% Efficiency via Perovskite Photovoltaics and Earth-Abundant Catalysts. *Science* **2014**, *345*, 1593−1596.

(9) Hu, X.; Zhang, X.; Liang, L.; Bao, J.; Li, S.; Yang, W.; Xie, Y. High-Performance Flexible Broadband Photodetector Based on Organolead Halide Perovskite. *Adv. Funct. Mater.* **2014**, *24*, 7373−7380.

(10) Xia, H.-R.; Li, J.; Sun, W.-T.; Peng, L.-M. Organohalide Lead Perovskite Based Photodetectors with Much Enhanced Performance. *Chem. Commun.* **2014**, *50*, 13695−13697.

(11) Lee, Y.; Kwon, J.; Hwang, E.; Ra, C.-H.; Yoo, W. J.; Ahn, J.-H.; Park, J. H.; Cho, J. H. High-Performance Perovskite-Graphene Hybrid Photodetector. *Adv. Mater.* **2015**, *27*, 41−46.

(12) Lin, Q.; Armin, A.; Lyons, D. M.; Burn, P. L.; Meredith, P. Low Noise, IR-Blind Organohalide Perovskite Photodiodes for Visible Light Detection and Imaging. *Adv. Mater.* **2015**, *27*, 2060−2064.

(13) Dou, L.; Yang, Y.; You, J.; Hong, Z.; Chang, W.-H.; Li, G.; Yang, Y. Solution-Processed Hybrid Perovskite Photodetectors with High Detectivity. *Nat. Commun.* **2014**, *5*, 5404.

(14) Dong, R.; Fang, Y.; Chae, J.; Dai, J.; Xiao, Z.; Dong, Q.; Yuan, Y.; Centrone, A.; Zeng, X. C.; Huang, J. High-Gain and Low-Driving-Voltage Photodetectors Based on Organolead Triiodide Perovskites. *Adv. Mater.* **2015**, *27*, 1912−1918.

(15) Guo, Y.; Liu, C.; Tanaka, H.; Nakamura, E. Air-Stable and Solution-Processable Perovskite Photodetectors for Solar-Blind UV and Visible Light. *J. Phys. Chem. Lett.* **2015**, *6*, 535−539.

(16) Jeon, N. J.; Noh, J. H.; Kim, Y. C.; Yang, W. S.; Ryu, S.; Seok, S. I. Solvent Engineering for High-Performance Inorganic−Organic Hybrid Perovskite Solar Cells. *Nat. Mater.* **2014**, *13*, 897−903.

(17) Agarwal, S.; Seetharaman, M.; Kumawat, N. K.; Subbiah, A. S.; Sarkar, S. K.; Kabra, D.; Namboothiry, M. A. G.; Nair, P. R. On the Uniqueness of Ideality Factor and Voltage Exponent of Perovskite-Based Solar Cells. *J. Phys. Chem. Lett.* **2014**, *5*, 4115−4121.

(18) Roelofs, K. E.; Brennan, T. P.; Dominguez, J. C.; Bailie, C. D.; Margulis, G. Y.; Hoke, E. T.; McGehee, M. D.; Bent, S. F. Effect of Al_2O_3 Recombination Barrier Layers Deposited by Atomic Layer Deposition in Solid-State CdS Quantum Dot-Sensitized Solar Cells. *J. Phys. Chem. C* **2013**, *117*, 5584−5592.

(19) Ip, A. H.; Quan, L. N.; Adachi, M. M.; McDowell, J. J.; Xu, J.; Kim, D. H.; Sargent, E. H. A Two-Step Route to Planar Perovskite Cells Exhibiting Reduced Hysteresis. *Appl. Phys. Lett.* **2015**, *106*, 143902.

(20) Wojciechowski, K.; Stranks, S. D.; Abate, A.; Sadoughi, G.; Sadhanala, A.; Kopidakis, N.; Rumbles, G.; Li, C.-Z.; Friend, R. H.; Jen, A. K.-Y.; Snaith, H. J. Heterojunction Modification for Highly Efficient Organic−Inorganic Perovskite Solar Cells. *ACS Nano* **2014**, *8*, 12701−12709.

DOI: 10.1021/acsphotonics.5b00164
ACS Photonics 2015, 2, 1117−1123

(21) Xu, J.; Buin, A.; Ip, A. H.; Li, W.; Voznyy, O.; Comin, R.; Yuan, M.; Jeon, S.; Ning, Z.; McDowell, J. J.; Kanjanaboos, P.; Sun, J.-P.; Lan, X.; Quan, L. N.; Kim, D. H.; Hill, I. G.; Maksymovych, P.; Sargent, E. H. Perovskite−fullerene Hybrid Materials Suppress Hysteresis in Planar Diodes. *Nat. Commun.* **2015**, *6*, 7081.
(22) Abrusci, A.; Stranks, S. D.; Docampo, P.; Yip, H.-L.; Jen, A. K.-Y.; Snaith, H. J. High-Performance Perovskite-Polymer Hybrid Solar Cells via Electronic Coupling with Fullerene Monolayers. *Nano Lett.* **2013**, *13*, 3124−3128.
(23) Heo, J. H.; Im, S. H.; Noh, J. H.; Mandal, T. N.; Lim, C.-S.; Chang, J. A.; Lee, Y. H.; Kim, H.; Sarkar, A.; Nazeeruddin, M. K.; Grätzel, M.; Seok, S. I. Efficient Inorganic−organic Hybrid Heterojunction Solar Cells Containing Perovskite Compound and Polymeric Hole Conductors. *Nat. Photonics* **2013**, *7*, 486−491.
(24) Pattantyus-Abraham, A. G.; Kramer, I. J.; Barkhouse, A. R.; Wang, X.; Konstantatos, G.; Debnath, R.; Levina, L.; Raabe, I.; Nazeeruddin, M. K.; Grätzel, M.; Sargent, E. H. Depleted-Heterojunction Colloidal Quantum Dot Solar Cells. *ACS Nano* **2010**, *4*, 3374−3380.
(25) Di Fisica, S. *Silicon-Based Microphotonics: From Basics to Applications*; IOS Press, 1999.
(26) Zimmermann, H. *Integrated Silicon Optoelectronics*, 2nd ed.; Springer, 2000.
(27) Rogalski, A. *Infrared Detectors*, 2nd ed.; CRC Press, 2011.
(28) Konstantatos, G.; Howard, I.; Fischer, A.; Hoogland, S.; Clifford, J.; Klem, E.; Levina, L.; Sargent, E. H. Ultrasensitive Solution-Cast Quantum Dot Photodetectors. *Nature* **2006**, *442*, 180−183.
(29) Konstantatos, G.; Clifford, J.; Levina, L.; Sargent, E. H. Sensitive Solution-Processed Visible-Wavelength Photodetectors. *Nat. Photonics* **2007**, *1*, 531−534.
(30) Jason Paul, C.. Colloidal Quantum Dot Schottky Barrier Photodiodes. Doctor of Philosophy, University of Toronto: Toronto, 2008.

DOI: 10.1021/acsphotonics.5b00164
ACS Photonics 2015, 2, 1117−1123